7-8-2019

Investigation of Through Thickness Microstructure and Mechanical Properties in Friction Stir Welded 7N01 Aluminum Alloy Plate

Xingxin Zhao
Beijing Jiaotong University

Zhiyong Yang
Beijing Jiaotong University

Joseph P. Domblesky
Marquette University, joseph.domblesky@marquette.edu

Jianmin Han
Beijing Jiaotong University

Zhiqiang Li
Beijing Jiaotong University

See next page for additional authors

Materials Science and Engineering : A, Vol. 760 (July 8, 2019): 316-327. DOI.

Investigation of Through Thickness Microstructure and Mechanical Properties in Friction Stir Welded 7N01 Aluminum Alloy Plate

Yingxin Zhao
School of Mechanical Electronic & Control Engineering, Beijing Jiaotong University, Beijing, 100044, China
Zhiyong Yang
School of Mechanical Electronic & Control Engineering, Beijing Jiaotong University, Beijing, 100044, China
Joseph P. Domblesky
Department of Mechanical Engineering Marquette University, Milwaukee, WI
Jianmin Han

School of Mechanical Electronic & Control Engineering, Beijing Jiaotong University, Beijing, 100044, China

Zhiqiang Li

School of Mechanical Electronic & Control Engineering, Beijing Jiaotong University, Beijing, 100044, China

Xiaolong Liu

School of Mechanical Electronic & Control Engineering, Beijing Jiaotong University, Beijing, 100044, China

Abstract

An on-going problem in friction stir welded (FSW) joints used in the high-speed train sector is that the microstructure and mechanical properties can significantly vary in thick sections. Because inhomogeneous properties can reduce weld efficiency and degrade service performance, it is of some interest to understand how inhomogeneous properties can develop in FSW welds made from precipitation hardening alloys such as 7N01. In the current study, butt welds were made using 12 mm thick plates and then sectioned perpendicular to the weld line. Five 2.2 mm thick slices were cut from a section and used to measure tensile properties access the weld thickness. The microstructure was characterized using scanning electron microscopy (SEM) and energy dispersive spectrometry (EDS) to measure variation in grain size and second phase particle distributions over the weld zone. Results showed that, with the exception of the top slice, yield strength (σ_y) and ultimate tensile strength (σ_{UTS}) obtained from the slices were fairly consistent and comparable to values from the full weld. Elongation (δ) was maximum at mid-thickness decreased significantly towards the crown. Although significantly reduced elongation was found at the top of the weld, and likely limits overall weldment ductility, elongation of the full FSW weld was improved over that of the base metal and can be attributed to enhanced post-necking straining. The finest grains and second phase particles were observed at mid-thickness. In comparison, the coarsest grains were observed at the top of the nugget. This microstructural variation can be understood by considering the temperature and strain field gradients that are generated in the plasticized zone. It is expected that the findings will help to promote a better understanding of post-weld microstructure development and mechanical properties of thick plates.

Keywords

Friction stir welding, Aluminum alloy, Microstructure, Mechanical properties, Second phase particles

1. Introduction

As engineering design requirements in the rail transportation sector continue to emphasize the development of light-weight, high-strength welded structures, the use of 7xxx series aluminum alloys has grown extensively. However, due to their high Cu content, most 7xxx alloys are difficult to join using conventional fusion welding as they are highly susceptible to the formation of weld and liquation cracks in the heat affected zone as well as significant degradation of mechanical properties in the weld zone [1,2]. Friction stir welding (FSW) has proven to be an enabling technique and has been successfully used to weld most precipitation-hardenable aluminum alloys including the 2xxx, 6xxx, and 7xxx series [[3], [4], [5], [6], [7]]. However, many structural applications in high speed rail cars involve joining thick plates (i.e. thickness greater than 6 mm) where non-uniform thermal-mechanical conditions often develop in the weld zone. As FSW weld microstructure is dependent on the thermal history [8,9] and material flow fields [10,11] created by the tool, thick plates often show significant variation

over the weld section. Because microstructural development is closely tied to joint performance, this variation can also have a deleterious effect on mechanical properties of the weldment.

Mechanical properties and microstructure of FSW welds made from thin sheets of precipitation hardened aluminum alloys (i.e. less than 6 mm thickness) have been studied by a number of researchers. These workers have extensively studied the thermal history [12], material flow patterns [13,14], microstructure evolution [15], and mechanical properties [16,17] in some detail. Their results show that as-welded mechanical properties tend to be relatively uniform for weldments made using this range of thickness. An increasing number of workers have also begun to study weld microstructure and properties in thicker sections (i.e. greater than 6 mm). Xu, W. et al. [18,19] investigated the through thickness microstructure and strain hardening properties of welds made using 14 mm thick AA2219 plate. They reported that a fine, equiaxed recrystallized grain structure developed at the top of the weld nugget zone (WNZ) while the grains and second-phase particles in the middle sections exhibited obvious signs of coarsening. Compared with the middle and bottom sections of the weld, the top had a higher strength but lower ductility and strain hardening capacity. Guo, N., et al. [20] tested welds made from 108 mm thick 5A06 aluminum alloy plates and their results showed that the grain size in the WNZ was maximum at the top and decreased gradually along the thickness direction. They cut the weld cross-section into slices and found that in the upper slice, the hardness value decreases significantly from the BM to the WNZ and the minimum hardness was observed at the weld center. For other slices, the hardness first decreased from the BM to the HAZ and then increased to the center of the WNZ such that the hardness profile showed a “W” shape. This suggests that tensile properties will also demonstrate a similar variation over the weld section. Canaday, C. T. et al. [21] carried out a study using 32-mm-thick AA7050 alloy plates and hypothesized that the mid-depth temperature in the nugget was higher due to ambient convection at the top surface and conduction to the backing plate. This was based on the observation that maximum grain size occurred at mid-plane with smaller grains near the root and crown. Martinez, N., et al. [[22], [23], [24]] observed that a significant heat gradient developed between the top and bottom of the nugget in 13-mm-thick 7449 aluminum welds resulting in microstructural variations over the nugget zone. They hypothesized that the top of the nugget had the highest heat input which resulted in a microstructure with high solid solution strengthening, larger grains, larger precipitates, and average dislocation density. In comparison, because less heat is generated at the bottom of the nugget, finer precipitates, finer grains, and a higher dislocation density were expected to develop. Mao, Y., et al. [25,26] carried out studies using 20-mm-thick AA7075 alloy plates and found that the temperature difference between the top and the bottom of the weld reached was on the order of 90 °C. They observed that the smallest average grain size and most homogeneous distribution of fine reprecipitated particles was in the middle-upper section of the weld. As a result, the tensile properties in the middle-upper had the highest ultimate tensile, yield strength, and elongation values compared to other sections.

From the literature, it is apparent that while some research work has been conducted on thick plates and 7xxx series alloys, some disparities remain regarding microstructure variation and heat distribution. Additionally, little information appears to have been published on microstructure and property variation in 7N01 aluminum alloy. In the present study, the aim was to study the formation of inhomogeneous microstructures and analyze how the variation of mechanical properties influenced performance thick plate FSW welds made from 7N01 alloy. Butt welds were made using 12-mm-thick 7N01 aluminum alloy plates and tensile properties were compared along the weld thickness using thin slices cut from a transverse section. Microstructure variation was evaluated using optical microscopy (OM) and electron back scattered diffraction (EBSD) to determine the grain size and grain distribution in the weld zone. Second phase particles distributions were characterized at different locations using scanning electron microscope (SEM) and energy dispersive spectrometer (EDS) techniques. A discussion of the resulting weld microstructure and inhomogeneity is presented along with the effects of tensile property variation on overall weld strength and efficiency. It is expected that the findings will help to promote a better understanding of post-weld microstructure development and mechanical properties of thick plates.

2. Material and experimental procedure

As 7N01 aluminum alloy is widely used in fabricating high speed rail car bodies, it was selected as the candidate material for this investigation. Alloy 7N01 is a heat-treatable Al–Mg–Zn alloy that was developed in Japan to specifically meet the design and manufacturing requirements for high-speed rail car frames and structures [27]. Alloy 7N01 has a slightly reduced Cu content in comparison to other 7xxx series and is specifically optimized for weldability and strength. The nominal chemical composition for 7N01 is given in Table 1.

Table 1. Chemical composition (expressed in Wt %) of the 7N01 aluminum alloy used in the study.

Al	Mg	Zn	Si	Fe	Mn	Cr	Ti
Bal	1.11	4.04	0.1	0.17	0.36	0.17	0.04

Base metal pieces were prepared by cutting 12-mm-thick cold rolled plates having a T4 temper into 300 mm × 100 mm sections. Butt welds were made using a China Center 3LM gantry type FSW machine which was equipped with a work-holding fixture and steel backing plate. A steel backing plate was used as it is standard on industrial FSW machines and it was desired to replicate conditions used in commercial welding. The FSW welding tool was made from hardened H-13 tool steel with a 37 mm diameter shoulder and a concave profile machined on the bottom side. A conical pin having a 14.8 mm shoulder diameter and 10° taper angle with an overall length of an 11.5 mm was used on the tool. The pin had a tri-lobular profile consisting of alternating flat surfaces and trapezoidal threads. The thread geometry was based on a 2 mm wide screw groove and 30° thread angle. A schematic of the FSW tool and relevant dimensions are shown in Fig. 1. The weld schedule used in the study was based on the results of a comprehensive series of welding trials that had been previously performed using 12 mm thick plate to ensure that sound, full-penetration welds were produced. All welds were 200 mm long and were made along the full length of the plates using a tool rotational speed of 350 rpm and travel speed of 300 mm/min. A plunge depth of 0.2 mm and a tilt angle of 2.5° were also applied to the tool during welding.

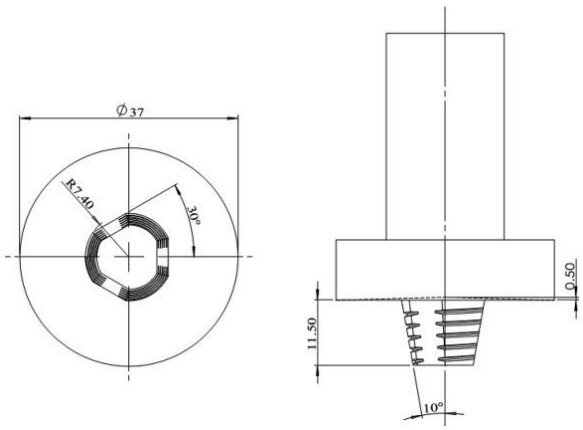

Fig. 1. Schematic drawing of the FSW tool used in the study. All dimensions given in mm.

After welding was completed, an electrical discharge machine (wire EDM) was used to cut transverse sections from the weldment. One of the sections was used to prepare tensile specimens that were used to test the mechanical properties of the bulk weld. A second section was cut into 2.2 mm thick slices which were also used to make tensile specimens to determine how tensile properties and ductility varied over the weld section. The surfaces and edges of all specimens were polished on a grinding wheel to minimize the possibility of any surface stress concentrations. Tensile testing was performed according to ISO 4136:2001 and ISO 6829-1:2009 standards using a 50 mm gage length and the specimen dimensions are shown in Fig. 2. All tensile tests were carried out at room temperature at a constant cross-head velocity of 1 mm/min on a SUNS 5305 testing machine. After tensile

testing was completed, the fracture surfaces of each tensile specimen were examined using a CamScan 3400 scanning electron microscope (SEM) to evaluate the failure mode.

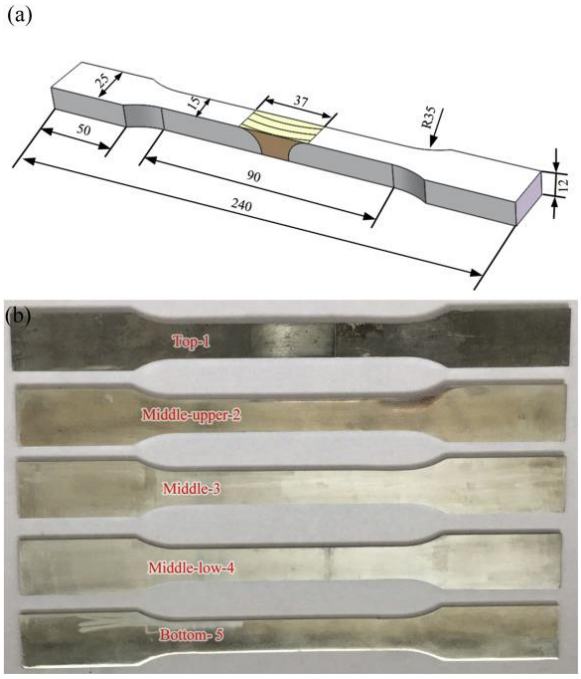

Fig. 2. Test specimens taken from the FSW weld showing: (a) tensile specimen and dimensions used to test bulk weld properties; and (b) photograph showing individual tensile bars prepared from the weld slices. All dimensions are given in mm.

One of the transverse sections was also used to conduct a microstructural analysis of the weld zone and adjacent base metal. After polishing and etching was performed using Keller's reagent, microstructural analysis of the precipitate particles was performed using an optical microscope (OM) and an SEM equipped with Oxford energy-dispersive X-ray spectroscopy (EDS). The grain size distribution of the weld microstructure was also examined using the electron backscattering diffraction (EBSD) technique. EBSD samples were cut from the weld joint transverse to the welding direction, and after undergoing standard grinding and mechanical polishing procedures, compound electrochemical polishing was carried out in a solution containing 10 vol% perchlorate acid and 90 vol% methanol at 300 K and 30 V for 15 s to eliminate the plastic-deformed region. EBSD measurements were then taken on a JSM-7001F system using a 20 kV acceleration voltage and a 2 μm step size.

3. Experimental results and discussion

3.1. Macrostructure and microstructure observation

Fig. 3 shows a macrograph taken from one of the transverse cross-sections and is representative of a typical aluminum FSW weld structure. Based on the observed macrostructure features, the weld joint can be seen to consist of four distinct zones which include a) weld nugget zone (WNZ), b) thermo-mechanically affected zone (TMAZ), c) heat-affected zone (HAZ) and d) surrounding base metal (BM). It can be seen that the shape of the WNZ is slightly asymmetric and can be attributed to the fact that higher temperatures are generated on the advancing side of the tool during welding. It can also be seen from Fig. 3 that the boundary between the TMAZ and WNZ is more optically distinct on the advancing side (AS) as compared to the retreating side (RS) of the weld. This can be explained by considering the prevailing direction of in-plane plastic flow on both sides of the weld pin relative to the travel direction. On the AS, the plasticized material being stirred moves in the direction of the tool travel and is subjected to a large shear force and shear deformation relative to the adjacent metal.

So, as a result of the steep deformation gradient and difference in internal energy, the boundary between the WNZ and TMAZ is more optically distinct. However, on the RS, the plasticized material is moving in the opposite direction and simply extrudes past the tool. Subsequently, a lower deformation gradient [28] is generated and the boundary is not as sharply defined.

Fig. 3. Photograph showing the four macroscopic weld zones.

Fig. 4 shows micrographs taken from each of the individual zones shown in Fig. 3. Aluminum and its alloys tend to exhibit very high rates of dynamic recovery and this is generally expected to inhibit dynamic recrystallization. However, the formation of new equiaxed grains in FSW welds made from Al alloys has been frequently reported in the literature [[29], [30], [31], [32]]. Three types of dynamic recrystallization processes are likely to produce equaxed grains in aluminum FSW welds and include: (i) discontinuous dynamic recrystallization (DDRX), i.e. classical recrystallization which operates by nucleation and grain growth; (ii) continuous dynamic recrystallization (CDRX), which involves the transformation of low angle boundaries into high angle boundaries; and (iii) geometric dynamic recrystallization (GDRX), generated by fragmentation of the initial grains [33].

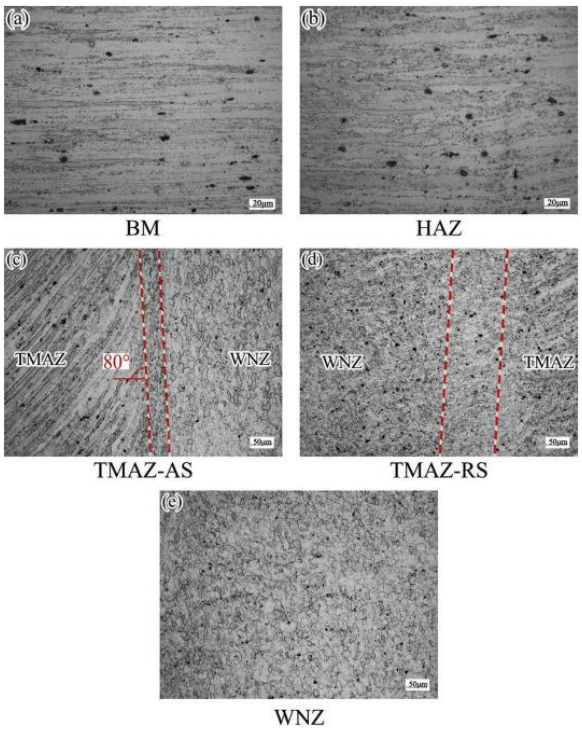

Fig. 4. Optical micrographs showing: (a) BM; (b) HAZ; (c) TMAZ in advancing side; (d) TMAZ in retreating side; (e) WNZ in the FSW weld joint.

The base metal microstructure of the 7N01 alloy in Fig. 4(a) exhibits large elongated grains which is typical of the morphology found in flat rolled plate. The black dots shown in Fig. 4 are second-phase particles and are

discussed in the next section. In the BM, the grains are highly elongated due to flat rolling and the lattice dislocations generated during cold working can either attain a low energy subgrain structure configuration or remain homogeneously dispersed within the grain interior [30]. As minimal heat or deformation is experienced by the surrounding BM material, insufficient driving force is available for recrystallization to occur. In the HAZ (Fig. 4(b)), the grain structure retains the same rolling morphology as the base metal, but here the grains also show evidence of slight coarsening owing to the effect of heat conduction from the WNZ.

The TMAZ microstructures, corresponding to the advancing side and retreating side of the weld, are shown in Fig. 4(c) and (d) respectively. While this material undergoes less deformation, evidence of significant shearing in the direction of tool rotation is evident on both the AS and RS. The material in the TMAZ experiences lower strains, strain rates, and temperatures compared to the WNZ and these conditions are not sufficient for recrystallization to occur. A clear transition region, highlighted by the dashed lines between WNZ and TMAZ in Fig. 4 (c) can also be observed on the advancing side of the weld. However, while a similar grain structure can be observed on the retreating side, the transition region is more widely distributed and is not as clearly defined. Some of the grains in the boundary region appear to have recrystallized and a duplex recrystallized grain structure is visible on the AS consisting of necklaced type grains which are characteristic of DDRX. As shown in Fig. 4(e), the WNZ is characterized by a distribution of fine equiaxed grains which indicates that the plasticized material in the weld nugget has undergone dynamic recrystallization due to the combined effect of strong plastic shearing and intense heat generation. Studies of microstructure evolution during processing and grain development [30] have shown that both CDRX and DDRX are operative during FSW. However, due to the fact that it was not feasible to observe the grain evolution during and after processing, the contribution of each mechanism could not be established in the FSW weldment.

3.2. Second-phases particles and distribution

Fig. 5 shows representative SEM images of second-phase particle distributions taken from the four different zones of the FSW weld. The second-phase particles can be clearly identified by the dark regions and surrounding white “bands”. The original precipitates in the BM (Fig. 5(a)) consist of a duplex mixture of fine and coarse particles which are elongated and oriented along the rolling direction. Based on the EDS microanalysis results shown in Fig. 6, the particles in the FSW joint mainly consist of η($MgZn_2$) phase and an Fe-rich phase [29]. In the HAZ (Fig. 5(b)), the second-phase particles appear to have coarsened slightly and also demonstrate less of an elongated appearance. In the TMAZ (Fig. 5(c)), most of the original particles on both side (AS and RS) have been broken up, dissolved, and re-precipitated out as relatively fine particles due to intense plastic deformation and resulting high temperatures. The dissolved and re-precipitated particles can generally be described as relatively fine and equiaxed in the WNZ. However, some variation was present and a range of particle sizes were observed over the weld. Consequently micrographs were taken at the top (Fig. 5(d)), middle (Fig. 5(e)), and bottom (Fig. 5(f)) of the nugget. Based on the micrographs of the WNZ, it can be seen that the precipitate particles in the middle are the smallest and most uniform in size and shape compared to those at the top and bottom. This is in variance with the hypothesis by Canaday et al. [21] that a high temperature region could develop at mid-depth. If this were the case, then the mid-weld region would experience the longest thermal cycle and significant coarsening of the precipitates would be expected at mid-depth of the WNZ. Observing the particles at the bottom of the WNZ, it can be seen that they have a duplex distribution of sizes and intermediate to those at the top and bottom of the nugget. While the precipitate particles at the top were found to be the largest of all three locations in the WNZ, a comparison of Fig. 5 (a) and 5 (d) confirms that they are still smaller than those found in the original BM plate material.

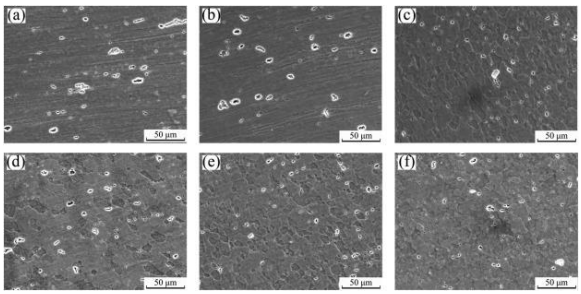

Fig. 5. SEM micrographs showing secondary phase particles of the joint: (a) BM; (b) HAZ; (c) TMAZ in advancing side; (d) WNZ-top; (e) WNZ-middle; (f) WNZ-bottom.

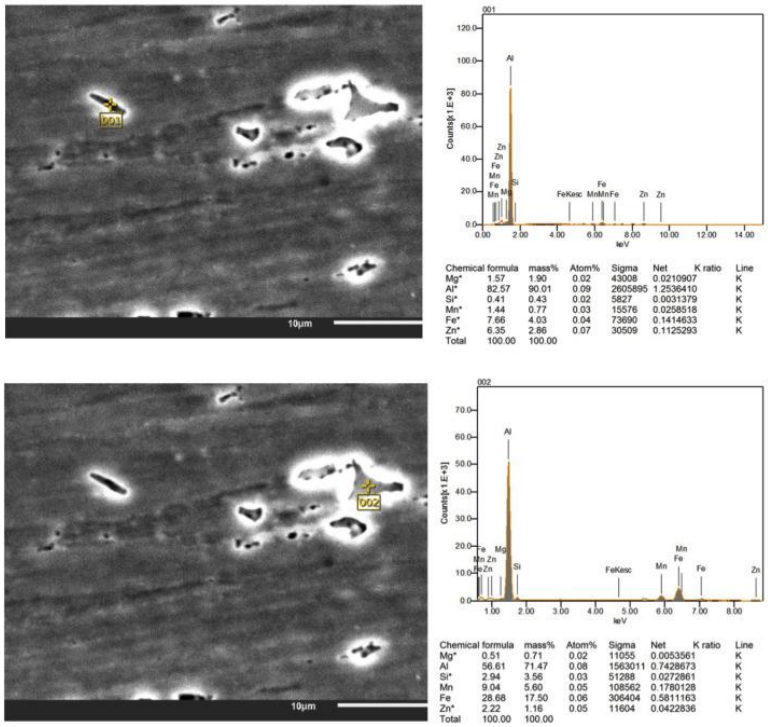

Fig. 6. EDS analyses results second-phase particles of FSW 7N01 Al alloy weld joint.

3.3. EBSD analysis

In an effort to more completely define the grain structure of the FSW weld joint, an EBSD analysis of the individual zones was performed to map out grain orientation. The resulting grain orientation maps obtained for the BM, HAZ, TMAZ, WNZ-top, WNZ-middle and WNZ-bottom zones of the FSW joint are shown in Fig. 7. Based on the EBSD analysis, the BM and HAZ both showed highly elongated, directional grain structures whereas the WNZ demonstrated equiaxed grains with no obvious directionality at all three locations (top, middle, and bottom). As expected, the TMAZ showed a mix of directional, elongated and equiaxed grains with a transition band of small, equiaxed grains. Fig. 8 shows an image quality (IQ) map of the joint with superimposed grain boundaries (colored according to misorientation angle. The grain boundaries can be divided into high angle grain boundaries (HAGBs) over 15° and low angle grain boundaries (LAGBs) ranging from 2° to 15°. As shown in Table 2, a large number of LAGBs were observed in the BM and these constituted 62.2% (due to the rolling process) of the total while the percentage of HAGBs was only found to be 37.8% or roughly one third. The percentage of LAGBs and HAGBs in the HAZ were found to be comparable with those observed in the BM. The TMAZ, which represents a transition area between the HAZ and WNZ, showed that the percentage of LAGBs decreased to

36.5% while HAGBs increased to 63.5%. The WNZ was found to have the highest percentage of HAGBs which was in excess of 70.0%.

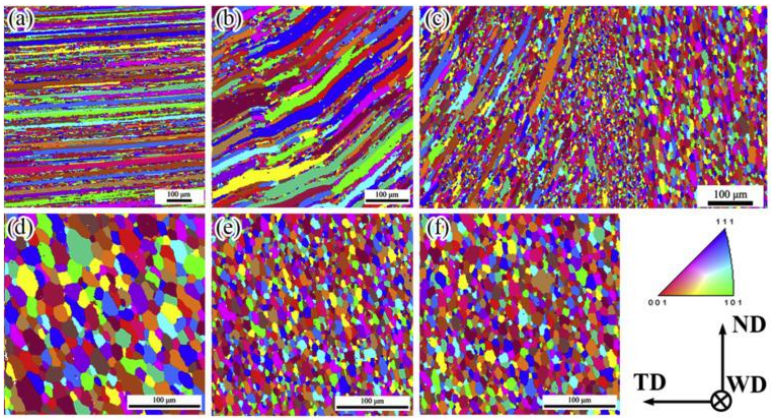

Fig. 7. EBSD orientation maps of the joint: (a) BM; (b) HAZ; (c) TMAZ in advancing side; (d) WNZ-top; (e) WNZ-middle; (f) WNZ-bottom.

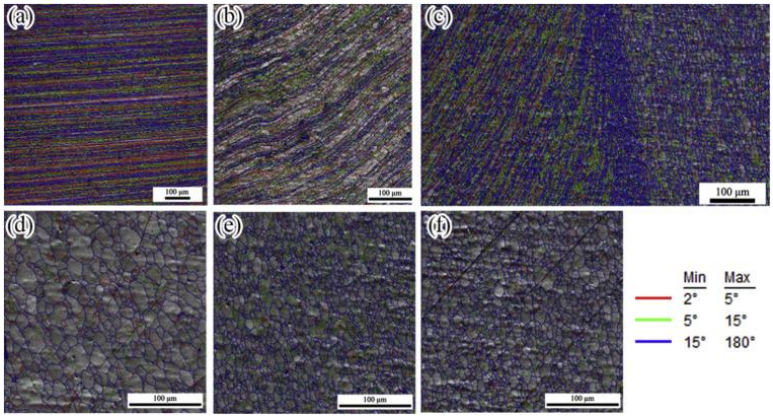

Fig. 8. EBSD image quality map of the joint: (a) BM; (b) HAZ; (c) TMAZ in advancing side; (d) WNZ-top; (e) WNZ-middle; (f) WNZ-bottom.

Table 2. Summary of average grain diameter and grain angle boundaries found in the FSW alloy 7N01 weld joint.

Detection Region	Average grain diameter (μm)	Percentage of LAGBs (%)	Percentage of HAGBs (%)
BM	6.37	62.2	37.8
HAZ	7.02	62.2	37.8
TMAZ	6.40	36.5	63.5
WNZ-top	11.03	42.5	57.5
WNZ-middle	6.16	34.2	65.8
WNZ-bottom	7.24	30.0	70.0

The average grain size in each region was also obtained using EBSD and the results are also summarized in Table 2. As shown in Table 2, the average grain diameter of the BM was determined to be 6.37 μm. While the resulting grain size in the weld zone ranged from 6.16 to 11.03 μm. Due to conductive heating in the HAZ, a notable amount of coarsening occurred and the grain size increased by about 10% to 7.02 μm. Although intense heat is generated during the FSW process, the average grain diameter in the HAZ increased from 6.37 to 7.02 μm but it was not sufficient to change the grain misorientation. This reflects the fact that this area only undergoes heating

and does not experience deformation. The EBSD results also showed that the grain diameter in the WNZ varied with depth with the coarsest grains (11.03 μm) being found at the top. The finest grain size (6.16 μm) was observed in the middle of the joint while the grain size at the bottom was intermediate and equal to 7.24 μm. This range of grain size in the WNZ is consistent with the very been reported fine structure (i.e. 1–10 μm) that has previously for AA7075 [[34], [35], [36]]. The grain size distribution in the WNZ shows some agreement with the one reported by Mao. et al. [25] for FSW welds made using AA7075. However, the results differ in that the largest grains in the study by Mao et al. were observed at the root, which is at variance with observations [37,38] that maximum heat generation occurs at the top adjacent to the tool shoulder and decreases proportionally with pin diameter. This heat gradient, along with conductive flow to the backing, infers that average grain size should monotonically decrease with weld depth and be minimum at the root.

To help understand the post-weld grain size distribution that develops in the WNZ, the strain field that develops in the plasticized region should also be considered in conjunction with temperature. A fundamental principle of recrystallization theory is that recrystallized grain size is inversely related to the amount of strain. While further study of the strain field and cooling history of the weld is warranted in thicker sections, finite element results published in Ref. [39] provide some insight regarding grain development in the WNZ for the 7N01 weld. The results obtained using an arbitrary Lagrangian Eulerian (ALE) based model show that the Von-Mises plastic strain for the WNZ is maximum at the crown and is minimum at the root. However the strain gradient in the upper half of the nugget was shown to be relatively small whereas the model showed that the gradient became significantly steeper in the bottom half of the weld with a more rapid drop-off in strain. Consequently, it can be expected that a small grain will develop in the crown region due to the peak strain and maximum temperature that develop. However, based on the high temperatures and large volume of plasticized metal generated by the shoulder, a longer cooling time is needed and it can be expected that substantial grain coarsening will occur. This has been verified by Hassan [40]. In comparison, at the root, the temperatures and the plastic strains are at a minimum. While these are still sufficient for recrystallization to occur, reduced nucleation rates will result and the resulting recrystallized grains can expect to have the maximum size out of the three locations in the WNZ. Furthermore, a shorter thermal cycle occurs as a result of thermal conduction between the steel backing plate and the bottom surface of the plate [41]. Due to conduction to the backing plate, a shorter thermal cycle occurs and minimal or reduced coarsening is likely. At the mid-section of the weld, if the strain values are comparable to the material at the top layers of the weld, a relatively fine grain can be expected. As the mid-section will cool more rapidly than the crown, less coarsening should result. Support for the idea that more rapid cooling occurs in the mid-section with minimal over-aging can be found in Fig. 5(e) and is evidenced by the smaller precipitates compared to Fig. 5(d).

3.4. Tensile properties

A longitudinal view of the fractured specimen obtained from a tensile test of the full weld is shown in Fig. 9. From Fig. 9 (a), it can be seen that the fracture lines follow the TMAZ with no fracture evident in any region of the WNZ. Examining Fig. 9 (b), a variation in transverse width can clearly be seen and confirms variation in properties over the weld. The characteristic saw tooth appearance resulting from the pin travel can be seen at the top of the weld in Fig. 9(b) and the adjacent, sub-surface material shows the maximum width and early evidence of fracture. Similar observations can be made at the root though the slightly narrower width indicates that initial crack development started later and required more strain to initiate. Based on the variation in width from the crown to middle-low section, it is evident that the latter had the maximum strength for the weldment and the final fracture occurred at that location.

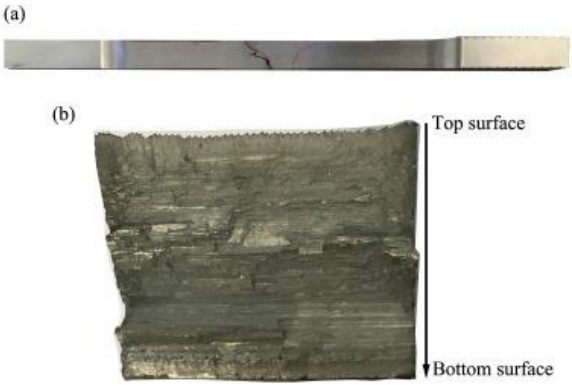

Fig. 9. Tensile result of transverse section of the full weld: (a) fracture position; (b) fracture surface.

Fig. 10 (a) shows the engineering stress-strain curves obtained from tensile tests conducted using the base metal (BM) and the five slices corresponding to different layers from the plate thickness. Fig. 10 (b) summarizes the corresponding values obtained for yield strength (σ_y), tensile strength (σ_{UTS}) and elongation (δ). The values of σ_y, σ_{UTS}, and δ obtained for the BM were found to be 325.67 MPa, 463.54 MPa and 15%, respectively. In comparison, a tensile test performed using a full transverse weld section showed that the resulting values for σ_y, σ_{UTS}, and δ were 253 MPa, 402 MPa, and 16.3% respectively after welding. Comparing both sets of values, σ_y has a 22% reduction while σ_{UTS} showed a 13% reduction for the full weld. This represents a notable reduction from the original BM strength. The resulting weld efficiency was calculated to be 87% which is typical for FSW made using 7xxx series aluminum alloys. However, it is interesting to note that while the FSW weld overall has lower yield and tensile strength than the BM, the effect of welding on ductility is actually somewhat beneficial as the elongation of the FSW weld increased by nearly 9%.

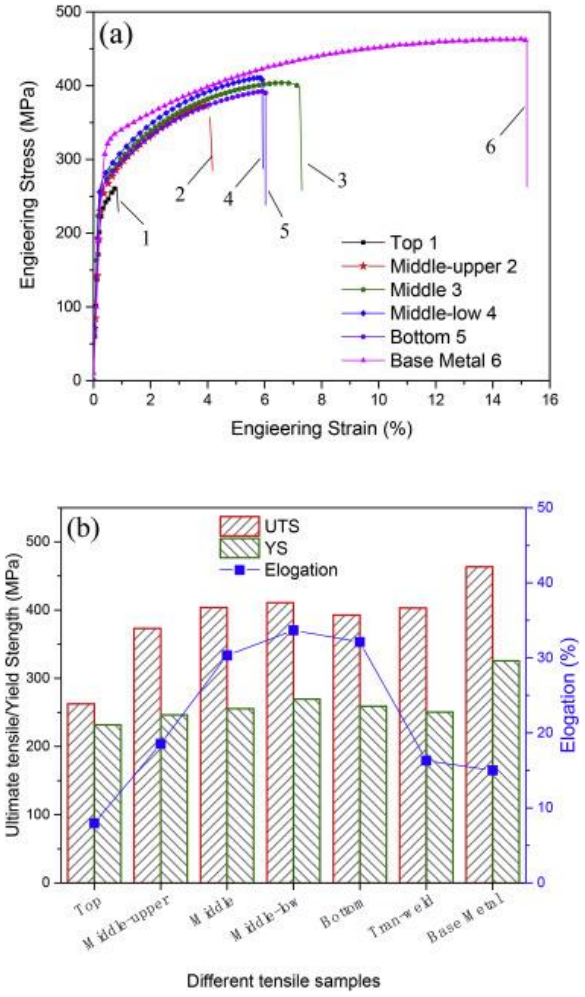

Fig. 10. Mechanical properties of the BM and joints: (a) stress–strain curves; (b) ultimate tensile, yield strength, and elongation diagrams.

While it is well known that weldment efficiency is reduced by FSW, it is of some interest to assess the performance of the individual slices and try to gain some insight into how each one contributes to the overall weld strength and performance. To facilitate this, comparisons of the tensile properties obtained for each individual slice are also shown in Fig. 10 (b) using a bar graph. It can be seen that, the σ_y and σ_{UTS} values of the individual slices showed a notable decrease from the BM. Except for the top slice, δ values showed a noticeable increase when compared to the BM. The maximum values of σ_y, σ_{UTS}, and δ that were obtained came from the weld middle-low slice (slice 4) and found to be 270 MPa, 411 MPa, and 33.7%, respectively. It can be seen that the values in the two adjacent slices (3, 5) were slightly lower but nonetheless are quite comparable. In comparison, slice 1 which was obtained from the top of the weld, had the lowest values of σ_y, σ_{UTS}, and δ which were 231 MPa, 262 MPa, and 7.9%, respectively. Slice 2 (middle-upper) appears to be somewhat of a transition section with tensile properties that are intermediate to those of slices 1 and 3.

Based on the tensile properties shown in Fig. 10 (b), it can be seen that all 5 slices have lower yield strength than the BM. However, all 5 slices have comparable σ_y values which are close to the yield strength of the weld and, as such, no single slice appears to have a negative effect on the yield strength of the weld section. However, while all five slices have σ_{UTS} values that are lower than the BM, it can be seen that the top slice has a significantly lower value compared to the other 4 slices. Comparison of slices 2–5 show that they are comparable to the σ_{UTS} obtained for the full weld. The value of σ_{UTS} in the top slice is 262 MPa, and represents a 42% reduction

compared to slice 2 which was 373 MPa. However the weldment σ_{UTS} is actually comparable to the values of slices 2–4 and suggest that the top slice has minimal negative effect on overall σ_{UTS}.

Comparing the elongation values of the individual slices, it can be seen that the top two slices (slice #1 and #2) demonstrated the lowest elongation values of 7.9% and 18.5% respectively. Although slice 1 is significantly lower, the elongation for the FSW weldment is comparable to that of slice 2. Consequently that δ values for slices 3–5 are in excess of 30%, this suggests that slice 1 is a limiting segment and that overall weld elongation could be enhanced by improving elongation in the material near the crown. It is well known that total elongation is governed by both pre and post-necking deformation [42], and while it is difficult to quantify the contribution of each slice to the overall weld, some insight can be gained. Based on the engineering stress-strain curve in Fig. 10 (a), it can be seen that the effect of FSW on post necking elongation is enhanced in slices 2–5. In comparison, it can be seen that the BM had very little post-necking capability. To verify this, the post-necking engineering strain $\varepsilon_{post\text{-}neck}$ was calculated for the individual slices and the BM:(1) $\varepsilon_{post-neck} = \frac{\varepsilon_{fracture} - \varepsilon_{UTS}}{\varepsilon_{UTS}}$

where $\varepsilon_{fracture}$ is strain when the sample is fractured, ε_{UTS} is the strain at the ultimate tensile strength. The $\varepsilon_{post\text{-}neck}$ found to be 0.016, 0.026, 0.089, 0.051, 0.019 and 0.009 respectively. Based on those values, FSW has a beneficial impact on post-necking strain and total elongation in the weldment.

Based on a comparison of the tensile properties of the individual slices shown in Fig. 10, the developed microstructure can be used to explain the behavior. In aluminum alloys, both grain size strengthening and precipitation hardening contribute to strength and both of these effects can occur in 7N01 alloy. The following model can take both effects into account:(2) $\sigma = \sigma_{BM} + \sigma_{HP} + \sigma_d$

where σ_{BM} is base matrix yield strength of pure Al, σ_{HP} is grain size strength and σ_d is precipitation strength. Although the individual effects are not easily quantifiable some observed can still be made. With respect to over-all strength, σ_{HP} , the Hall-Petch equation can be used to describe grain size contribution:(3) $\sigma_c = \sigma_0 + kd^{-1/2}$where σ_c is the strengthening stress which corresponds to yield stress; σ_0 and k are constants associated with the materials; and d is grain size. Based on Eq. (3), the smaller the grain size is, the higher the alloy yield strength will be. As shown in Table 2, the average grain diameter in the top of WNZ is 11.03 μm, which is much larger than those at the middle and bottom (6.16 μm and 7.24 μm, respectively). This result is also demonstrated by the tensile properties where the yield strength of the top of the weld has a lower effect compared to the middle and bottom positions. However, this is likely only a minor portion of the flow stress difference based on the relatively small differences in the grain size.

As seen in Eq. (2), precipitation hardening also influences the tensile properties and has a profound effect. According to previous research, precipitation strengthening is the primary strengthening mechanism in 7xxx alloys [43,44]. The metastable η($MgZn_2$) phase and Fe-rich phase are the main strengthening phase of 7N01 alloy according to Fig. 10. It is well established that the higher of precipitation density and smaller of precipitated particle size is, the higher of alloy yield strength is. As shown in Fig. 5 (d–f), the coarsest second phase particle size and density was in the top slice (Top-1). In comparison, the middle and bottom slices demonstrate higher levels of mechanical strength due to the smaller grain and precipitated particle size.

As the ability to withstand plastic deformation during overload conditions is an important consideration for many structures; the strain hardening exponent, percent uniform elongation and the yield to tensile stress ratio are commonly used as metrics to assess the capability to withstand plastic deformation prior to the onset of necking. These dimensionless parameters are collectively known as the plastic deformation index [45] and represent important metrics used for material specification and design integrity analyses. From a design standpoint, one interpretation of *Hc* is that it represents the overload capacity of a material or member during uniform deformation. As such, a higher numerical value indicates a greater ability to handle stresses prior to the

onset of unstable deformation. However, a second interpretation is that many ductile materials tend to have a smaller difference between the yield and tensile strengths such that a low value would indicate better capability to withstand plastic deformation prior to instability. As both properties are important in rail car structures it thus useful to consider *Hc* as a measure of weldment strength and to employ alternative metrics to describe stable plastic strain. The strain hardening capacity (*Hc*) of material can be defined as the ratio of the yield strength to the ultimate tensile strength [19,46] and is frequently expressed as a normalized parameter as follows:(4) $Hc = \frac{\sigma_{UTS} - \sigma_y}{\sigma_y} = \frac{\sigma_{UTS}}{\sigma_y} - 1$

The strain hardening exponent, which is typically used to represent in the Hollomon relationship is also frequently employed to measure stable deformation. Based on Considere's criterion, it has been shown that the strain hardening exponent is equal to the true strain that occurs prior to necking in a tensile test. As such, a larger value of the strain hardening exponent for a material indicates that it can undergo greater amounts of the plastic strain prior to the onset of instability in simple tension. The Hollomon equation [47] is usually stated as:(5) $\sigma = K\varepsilon^n$ where *n* is the strain hardening exponent, *K* is the strength coefficient, σ is the true stress and ε is the true strain. Several workers [48,49] have criticized the use of Eq. (5) as a means to find the instability strain based on the argument that it predicts stress values even at low values of strains. However, the following points should be considered. The first is that the power law is an empirical curve fit and *n* is used to describe the rate of strain hardening which can vary with strain for a given material. In any event, *n* should be calculated based on data taken between σ_y and σ_{UTS}. The second point is that the calculation of the instability strain using *n* assumes proportional loading conditions consistent with those for uniaxial tension were maintained during testing. However, while proportional loading conditions can be met using rectangular specimens, the stress and strain proportions will not be the same as those achieved during uniaxial tension for a cylindrical round rod. As such, suitable caution must be exercised when trying to establish the amount of stable straining using rectangular tensile specimens. Such values do nonetheless represent a useful means for making relative comparisons.

The results obtained for the hardening capacity and strain hardening exponent are shown in Fig. 11 for the individual slices and BM. The strain hardening exponents (i.e. “n”) were determined from the slopes of $ln\sigma - ln\varepsilon$ plots that were using data points between yield and necking. The hardening capacity of the full FSW weld and BM were also calculated and found to be 0.59 and 0.42, respectively. This indicates that while weld efficiency is reduced compared to the BM, *Hc* is notably improved and overloading capacity is increased. Although the *Hc* of slice 1 is significantly lower that slices 2–5, it does not have an adverse effect on the overall weld. The higher n values in slices 2–5 reflect the fact that the FSWed joints had a fine and equiaxed grain in the WNZ leading to a higher strain hardening rate in comparison with the BM. It can also be seen from Fig. 11 that the top slice has the lowest strain hardening exponent which indicates it has the least capacity for stable deformation and can be attributed to the coarse, overaged microstructure in this area. Similarly, there is larger grain size in the top slice caused lower strain hardening rate compare with other slices. With the exception of the top slice, the strain hardening capacity and strain hardening exponent for slices 2–5 are all higher compared to the base metal.

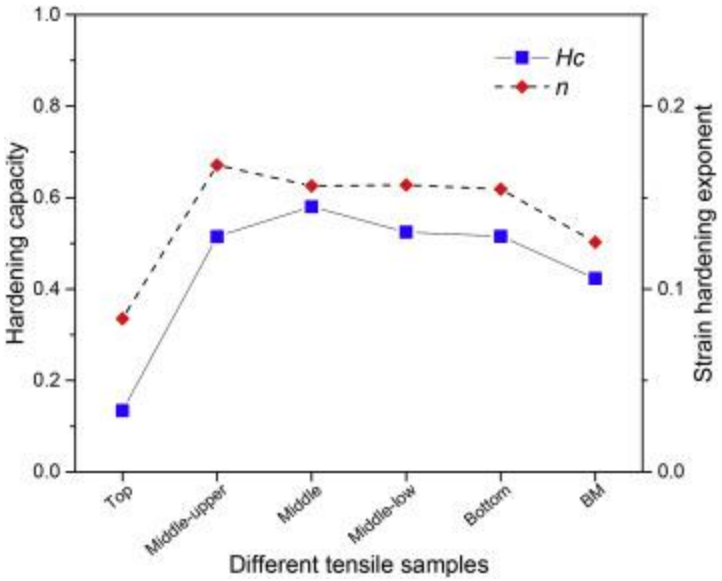

Fig. 11. Comparisons of strain hardening capacity (*Hc*) and strain hardening exponent (*n*) for different slices and base metal.

3.5. Fracture morphology

To analyze the failure mode of the individual slices, the fracture surfaces of the tensile specimens corresponding to the top, middle and bottom weld slices were evaluated by SEM. For the top slice, tensile specimens fractured through the WNZ in 45° shear mode (Fig. 12 (a)) and numerous small dimples can be seen in the accompanying high-magnification photograph (Fig. 12 (b)). This is consistent with the fact that the lowest elongation value observed for the top slice and that plastic deformation capability was reduced. Fig. 12 (c) shows the fracture surfaces in the middle slice, which indicates that the fracture is ductile due to the presence of tear ridge and dimples. Compared with the dimples observed in the top slice, the dimples observed in Fig. 12 (d) are larger and deeper in depth which indicates that the material at this depth has higher plasticity and toughness. For the bottom slice, the fracture position was located in the HAZ. The microstructure exhibits show an obvious fibrous structure and the fracture plane mainly consist of elongated dimples (shown in Fig. 12 (e) and (f)) which reflect the flat rolled microstructure of the BM.

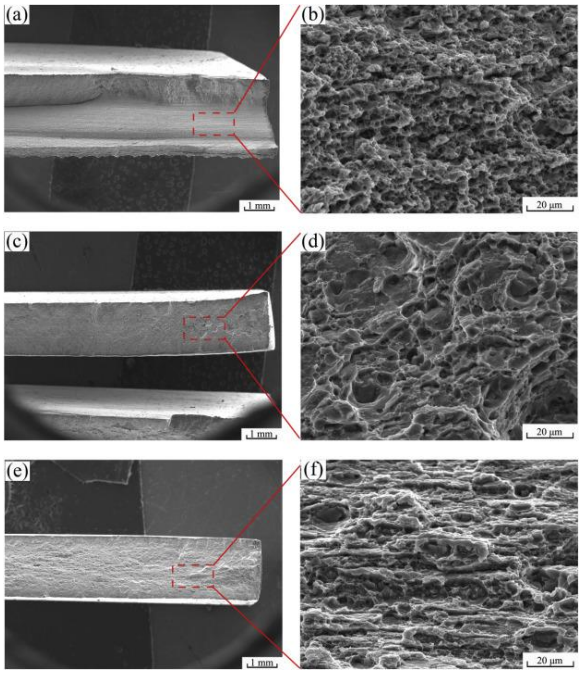

Fig. 12. SEM images of the slice specimens: (a) top, (c) middle, and (e) bottom; (b), (d) and (f) show high-magnification graphs of the region, indicated by the rectangular box in (a), (c) and (e).

The variation in fracture locations is consistent with the microstructural features when heat flow during FSW is considered. Based on the coarse grains and precipitates, it is not surprising that failure occurred in the WNZ rather than in the adjacent material for the top of the weld. Failure also occurred in the WNZ in the middle slice but can be explained by considering that while slightly larger precipitates were present in the HAZ and grain sizes in the HAZ and WNZ were quite close. It can be expected that the longer thermal cycle will cause substantial recovery in the recrystallized grains which will be more highly annealed than the HAZ. At the bottom of the weld significant heat flow to the backing plate will occur from the HAZ and WNZ such that relatively low levels of annealing would be expected. Here though the WNZ material will undergo some work hardening even after the pin has passed a given position [29]. This coupled with the relatively finer precipitates in the WNZ will provide a higher level of strength relative to the HAZ in the slice.

4. Summary and conclusions

In the present work, an experimental investigation of friction stir welded 12 mm thick 7N01 aluminum alloy plate was conducted. The effect of through thickness variation related to microstructure evolution and mechanical properties was compared and studied using thin slices which were also used to assess the contribution of each slice to overall weld performance. Based on the results of this investigation, the following can be concluded:

1. FSW led to significant microstructural changes both across the weld and in the thickness direction. The initial rolling structure of the BM was replaced by fine, equiaxed recrystallized grains in the WNZ. The minimum average grain size was found in the middle of WNZ and was about 6.16 μm whereas the maximum grain size of 11.03 μm was deserved in the top.
2. The second phase particles in the FSW joint are mainly $\eta(MgZn_2)$ phase and an Fe-rich phase. Within the WNZ, the precipitated particles in the middle zone are smaller and more uniform compared to those at the top and bottom for the same joint. This variation is likely due to the thermal gradient and inhomogeneous strain that is generated during FSW welding.

3. The lowest mechanical properties were found at the top of the weld. Analysis of the remaining slices showed that maximum tensile properties occurred at the middle-lower section and while the adjacent slices had slightly lower values, they were found to have comparable properties.
4. The fracture morphologies show that most of the individual slice failures are ductile. The largest and deepest dimples were observed in the middle of the weld which also had the highest elongation value.
5. The efficiency of 7N01 FSW weld was found to be 87%. While yield and tensile strength were reduced from the base metal values, elongation of the full weld was slightly enhanced due to increased capacity for post neck deformation.

Acknowledgements

This work was supported by the National Natural Science Foundation of China (No. 11802011), the Joint Funds of the National Natural Science Foundation of China (No. U1834202), the National Key Research and Development Program of China (No. 2017YFB0702004), the 973 Programs (No. 2015CB654805), the Fundamental Research Funds for the Central Universities (No. 2017RC028), and the National Key Technology R&D Program (No. 2015BAG12B01-09) are acknowledged.

References

[1] M. Prapas, N. Jennarong, P. Woraphot, J. Wuhan Univ. Technol.-Materials Sci. Ed., 32 (2017), pp. 1420-1425
[2] M. Nicolas, A. Deschamps, Metall. Mater. Trans. A-Phys. Metall. Mater. Sci., 35A (2004), pp. 1437-1448
[3] C. Vidal, V. Infante, J. Mater. Eng. Perform., 22 (2013), pp. 2261-2270
[4] F. De Geuser, B. Malard, A. Deschamps, Phil. Mag., 94 (2014), pp. 1451-1462
[5] S. Baragetti, G. D'Urso, J. Mech. Sci. Technol., 28 (2014), pp. 867-877
[6] A. Dorbane, G. Ayoub, B. Mansoor, R.F. Hamade, A. Imad, J. Mater. Eng. Perform., 26 (2017), pp. 2542-2554
[7] C. Deng, H. Wang, B. Gong, X. Li, Z. Lei, Int. J. Fatigue, 83 (2016), pp. 100-108
[8] M. Khandkar, J. Khan, A. Reynolds, Sci. Technol. Weld. Join., 8 (2003), pp. 165-174
[9] W. Xu, J. Liu, G. Luan, C. Dong, Mater. Des., 30 (2009), pp. 1886-1893
[10] G.Q. Chen, Q.Y. Shi, Y. Fujiya, T. Horie, J. Mater. Eng. Perform., 23 (2014), pp. 1321-1328
[11] S.D. Ji, Y.Y. Jin, Y.M. Yue, S.S. Gao, Y.X. Huang, L. Wang, J. Mater. Sci. Technol., 29 (2013), pp. 955-960
[12] S. Verma, Meenu, J.P. Misra, Mater. Today: Mater.Today Proc., 4 (2017), pp. 1350-1356
[13] T. Tanaka, T. Hirata, N. Shinomiya, N. Shirakawa, J. Mater. Process. Technol., 226 (2015), pp. 115-124
[14] Y. Morisada, T. Imaizumi, H. Fujii, Sci. Technol. Weld. Join., 20 (2015), pp. 130-137
[15] T. Wang, Y. Zou, K. Matsuda, Mater. Des., 90 (2016), pp. 13-21
[16] Z.H. Zhang, W.Y. Li, J.L. Li, Y.J. Chao, Int. J. Adv. Manuf. Technol., 73 (2014), pp. 1213-1218
[17] G. Singh, K. Singh, J. Singh, Exp. Tech., 38 (2014), pp. 63-71
[18] W. Xu, J. Liu, D. Chen, J. Mater. Sci. Technol., 31 (2015), pp. 953-961
[19] W.F. Xu, J.H. Liu, D.L. Chen, G.H. Luan, J.S. Yao, Mater. Sci. Eng. A, 548 (2012), pp. 89-98
[20] N. Guo, Y. Fu, Y. Wang, Q. Meng, Y. Zhu, Mater. Des., 113 (2017), pp. 273-283
[21] C.T. Canaday, M.A. Moore, W. Tang, A.P. Reynolds, Mater. Sci. Eng. A, 559 (2013), pp. 678-682
[22] N. Martinez, N. Kumar, R.S. Mishra, K.J. Doherty, J. Alloy. Comp., 713 (2017), pp. 51-63
[23] N. Martinez, N. Kumar, R.S. Mishra, K.J. Doherty, Mater. Sci. Eng. A, 684 (2017), pp. 470-479
[24] N. Martinez, N. Kumar, R.S. Mishra, K.J. Doherty, J. Mater. Sci., 53 (2018), pp. 9273-9286
[25] M. Yuqing, K. Liming, L. Fencheng, C. Yuhua, X. Li, Int. J. Adv. Manuf. Technol., 86 (2016), pp. 141-154
[26] Y. Mao, L. Ke, F. Liu, Q. Liu, C. Huang, L. Xing, Mater. Des., 62 (2014), pp. 334-343
[27] A.K. Sachdev, R.K. Mishra, A. Mahato, A. Alpas, **Vehicle Lightweighting: Challenges and Opportunities with Aluminum.** Springer International Publishing (2012)
[28] O. Lorrain, J. Serri, V. Favier, H. Zahrouni, M. El, H. Volume, J. Mech. Mater. Struct., 4 (2009), pp. 351-369

[29] J.Q. Su, T.W. Nelson, R. Mishra, M. Mahoney, Acta Mater., 51 (2003), pp. 713-729
[30] K.V. Jata, S.L. Semiatin, Scripta Mater., 43 (2000), pp. 743-749
[31] J.-H. Cho, W. Jae Kim, C. Gil Lee, Mater. Sci. Eng. A, 597 (2014), pp. 314-323
[32] S.M. Bayazid, H. Farhangi, H. Asgharzadeh, L. Radan, A. Ghahramani, A. Mirhaji, Mater. Sci. Eng. A, 649 (2016), pp. 293-300
[33] S. Gourdet, F. Montheillet, Mater. Sci. Eng. A, 283 (2000), pp. 274-288
[34] J. Zhang, P. Upadhyay, Y. Hovanski, D.P. Field, Metall. Mater. Trans. A, 49 (2018), pp. 210-222
[35] K. Shojaei, S.V. Sajadifar, G.G. Yapici, Mater. Sci. Eng. A, 670 (2016), pp. 81-89
[36] M. Moghaddam, A. Zarei-Hanzaki, M.H. Pishbin, A.H. Shafieizad, V.B. Oliveira, Mater. Char., 119 (2016), pp. 137-147
[37] T.S. Rao, S.R.K. Rao, G.M. Reddy, Mater. Werkst., 49 (2018), pp. 851-858
[38] C.M. Chen, R. Kovacevic, Int. J. Mach. Tool Manuf., 43 (2003), pp. 1319-1326
[39] O. Lorrain, J. Serri, V. Favier, H. Zahrouni, M. El Hadrouz, J. Mech. Mater. Struct., 4 (2009), pp. 351-369
[40] K.A.A. Hassan, A.F. Norman, D.A. Price, P.B. Prangnell, Acta Mater., 51 (2003), pp. 1923-1936
[41] Y.J. Chao, X. Qi, W. Tang, J. Manuf. Sci. Eng., 125 (2003), pp. 138-145
[42] G. Qian, Y. Cao, M. Niffenegger, Y.J. Chao, W. Wu, Eur. J. Mech. A Solid., 69 (2018), pp. 135-146
[43] S. Yan, H. Chen, Z. Zhu, G. Gou, Mater. Des., 61 (2014), pp. 160-167
[44] M. Dixit, R.S. Mishra, K.K. Sankaran, Mater. Sci. Eng. A, 478 (2008), pp. 163-172
[45] B. Ma, J. Shuai, J. Fail. Anal. Prev., 18 (2018), pp. 508-518
[46] S.Q. Wang, J.H. Liu, D.L. Chen, Mater. Des., 56 (2014), pp. 174-184, (1980-2015)
[47] J.H. Hollomon, Trans. Metall. Soc. AIME, 162 (1945), pp. 268-290
[48] N. Afrin, D.L. Chen, X. Cao, M. Jahazi, Scripta Mater., 57 (2007), pp. 1004-1007
[49] W. Woo, L. Balogh, T. Ungár, H. Choo, Z. Feng, Mater. Sci. Eng. A, 498 (2008), pp. 308-313